Biosciences Division
Seibert, Marvin; Uppsala University, Department of Cell and Molecular Biology, Molecular Biophysics
Seuring, Carolin; Center for Free Electron Laser Science
Stellato, Francesco; Center for Free Electron Laser Science
Tilp, Thomas; Center for Free Electron Laser Science
Eisenberg, David; University of California, Howard Hughes Medical Institute
Messerschmidt, Marc; SLAC National Accelerator Laboratory, Linac Coherent Light Source
Williams, Garth; SLAC National Accelerator Laboratory, Linac Coherent Light Source
Koglin, Jason; SLAC National Accelerator Laboratory, Linac Coherent Light Source
Makowski, Lee; Northeastern University, Department of Bioengineering
Millane, Rick; University of Canterbury, Department of Electrical and Computer Engineering
Forsyth, Trevor; Institut Laue-Langevin; Keele University, EPSAM/ISTM
Boutet, Sébastien; SLAC National Accelerator Laboratory, Linac Coherent Light Source
White, Thomas; Center for Free Electron Laser Science
Barty, Anton; Center for Free Electron Laser Science
Chapman, Henry; Center for Free Electron Laser Science; University of Hamburg, Department of Physics
Chen, Swaine; National University of Singapore, Department of Medicine; Genome Institute of Singapore
Liang, Mengning; SLAC National Accelerator Laboratory, Linac Coherent Light Source
Neutze, Richard; Goteborgs universitet Naturvetenskapliga Fakulteten, Department of Chemistry and Molecular Biology
Robinson, Robert; Institute of Molecular and Cell Biology; National University of Singapore, Department of Biochemistry; Okayama University, Research Institute for Interdisciplinary Science

Keywords: X-ray fiber diffraction, XFEL, Filament systems

Flow-aligned, single-shot fiber diffraction using a femtosecond X-ray free-electron laser

David Popp[1], N. Duane Loh[2,3], Habiba Zorgati[1,4], Umesh Ghoshdastider[1], Lu Ting Liow[5], Magdalena I. Ivanova[6], Mårten Larsson[1], Daniel P. DePonte[7], Richard Bean[8], Kenneth R. Beyerlein[8], Cornelius Gati[8], Dominik Oberthuer[8,9], David Arnlund[10], Gisela Brändén[10], Peter Berntsen[10], Duilio Cascio[11], Leonard M. G. Chavas[8], Joe P. J. Chen[12,12a], Ke Ding[1], Holger Fleckenstein[8], Lars Gumprecht[8], Rajiv Harimoorthy[10], Estelle Mossou[13,14], Michael R. Sawaya[11], Aaron S. Brewster[15], Johan Hattne[15], Nicholas K. Sauter[15], Marvin Seibert[16], Carolin Seuring[8], Francesco Stellato[8], Thomas Tilp[8], David S. Eisenberg[11], Marc Messerschmidt[7], Garth J. Williams[7], Jason E. Koglin[7], Lee Makowski[17], Rick P. Millane[12], Trevor Forsyth[13,14], Sébastien Boutet[7], Thomas A. White[8], Anton Barty[8], Henry Chapman[8,18], Swaine L. Chen[5,19], Mengning Liang[8], Richard Neutze[10], and Robert C. Robinson[1,4,20].

***1 - Institute of Molecular and Cell Biology**, Biopolis, A*STAR (Agency for Science, Technology and Research), Singapore 138673.*

***2 - Department of Physics, National University of Singapore,** Singapore 117557.*

***3 – Centre for BioImaging Sciences, National University of Singapore,** Singapore 117546.*

***4 - Department of Biochemistry, National University of Singapore,** Singapore 117597.*

***5 - Department of Medicine, National University of Singapore**, Singapore 119074.*

***6 - University of Michigan, Dept. of Neurology,** 109 Zina Pitcher Pl., Ann Arbor, MI 48109.*

***7 - Linac Coherent Light Source, SLAC National Accelerator Laboratory**, 2575 Sand Hill Road, Menlo Park, CA 94025, USA.*

***8 - Center for Free Electron Laser Science,** DESY, Notkestrasse 85, Hamburg, 22607, Germany.*

***9 - Institute of Biochemistry and Molecular Biology, University of Hamburg**, Hamburg 22607, Germany.*

***10 - Department of Chemistry and Molecular Biology, University of Gothenburg,** 405 30 Gothenburg, Sweden.*

***11 - Howard Hughes Medical Institute, University of California**, Los Angeles, CA 90095, USA.*

***12 - Computational Imaging Group, Department of Electrical and Computer Engineering, University of Canterbury**, Christchurch, New Zealand.*

12a – Present address: Department of Physics, ASU, USA

***13 - Institut Laue-Langevin,** Grenoble, 38000, France.*

***14 - EPSAM/ISTM, Keele University**, Staffordshire, ST5 5BG, UK.*

***15 - Physical Biosciences Division, Lawrence Berkeley National Laboratory,** Berkeley, CA 94720, USA.*

***16 - Department of Cell and Molecular Biology, Molecular Biophysics, Uppsala University**, 751 24 Uppsala, Sweden.*

17 - Department of Bioengineering, Northeastern University, *360 Huntington Ave, Boston, MA 02115, USA.*

18 - Department of Physics, University of Hamburg*, Luruper Chaussee 149, Hamburg 22607, Germany.*

19 - Genome Institute of Singapore, *Biopolis, A*STAR (Agency for Science, Technology and Research), Singapore 138672.*

20 - Research Institute for Interdisciplinary Science, *Okayama University, Okayama 700-8530, Japan.*

Address correspondence to: Robert C. Robinson. Institute of Molecular and Cell Biology, Proteos 61 Biopolis Drive, 138673, Singapore. Tel: +65869877; Fax: +6567791117; E-mail: rrobinson@imcb.a-star.edu.sg

Abstract

A major goal for X-ray free-electron laser (XFEL) based science is to elucidate structures of biological molecules without the need for crystals. Filament systems may provide some of the first single macromolecular structures elucidated by XFEL radiation, since they contain one-dimensional translational symmetry and thereby occupy the diffraction intensity region between the extremes of crystals and single molecules. Here, we demonstrate flow alignment of as few as 100 filaments (*E. coli* pili, F-actin, and amyloid fibrils), which when intersected by femtosecond X-ray pulses result in diffraction patterns similar to those obtained from classical fiber diffraction studies. We also determine that F-actin can be flow-aligned to a disorientation of ~5 degrees. Using this XFEL-based technique, we determine that gelsolin amyloids are comprised of stacked β-strands running perpendicular to the filament axis, and that a range of order from fibrillar to crystalline is discernable for individual α-synuclein amyloids.

Key words: XFEL, fiber diffraction, filament systems

Introduction

Fiber diffraction has a long history in being used to determine the structures of biological filaments. In the early 1920's Michael Polanyi adapted the earlier advances in X-ray diffraction studies [Friedrich et al., 1912; Bragg, 1913] to study natural fibers, such as cellulose, and formulated a theoretical concept of fiber diffraction [Polanyi et al., 1921; Polanyi et al., 1923]. X-ray fiber diffraction studies of tobacco mosaic virus (TMV) by Bernal and Fankuchen followed in the early 1940s [Bernal and Fankuchen, 1941]. Yet X-ray fiber diffraction, as we know it, only started in the 1950s, most notably with the determination of the primary double helical structure of DNA [Wilkins et al., 1953; Franklin and Gosling, 1953; Watson and Crick, 1953]. In 1958, Klug and collaborators produced the formalism that allowed a three dimensional density map to be calculated from fiber diffraction data [Klug et al., 1958]. However, only a limited number of filament systems have given rise to high quality fiber diffraction patterns suitable for solving structures at near atomic resolution, such as in the cases of TMV [Namba and Stubbs, 1986] and flagella [Yamashita et al., 1998a].

In fiber diffraction, the X-ray diffraction pattern is unchanged as the sample is rotated around the fiber axis, which is a result of the random rotations of the constituent molecules about this axis. Additionally, many polymers repeat periodically along their lengths confining the scattering to layer lines of helical polymers. The intensity distribution along the layer lines is best expressed as a sum of Bessel functions of integer order [Holmes and Blow, 1965]. Yet, only in rare cases do fibers naturally align to produce high quality fiber diffraction patterns, such as in muscle fibers [Huxley, 1953]. For biopolymers that are semi-rigid or more flexible *in vivo*, the preparation of oriented, and sometimes polycrystalline, fiber specimens *in vitro* have also allowed the application of fiber diffraction analysis for structure determination [Arnott, 1980; Millane, 2001]. Success depends critically on the accuracy of specimen orientation, which has proven to be the major bottleneck for structure determination by fiber diffraction. In all cases, preparing oriented sols with a small enough disorientation standard deviation required the protein concentration to be greater than 100 mg/ml and the viscosities to be low enough to allow flow orientation in a glass capillary. Other factors such as filament length, ionic conditions, pH, and application

of high magnetic fields can also play important roles in the orientation process [Yamashita et al., 1998b; Oda et al., 2009]. In practice, a large amount of protein (>1 g) has been needed to optimize the process of orientation before useful X-ray fiber diffraction data were obtained [Popp et al., 1987].

To circumvent the practical limitations of preparing sols of oriented filaments, we used flow-alignment through a gas dynamic virtual nozzle (GDVN). Here, a co-axial helium gas flow acts as a virtual nozzle that focuses the liquid jet and by accelerating the fluid, the cross section of the liquid jet is reduced (Fig. 1; Supplementary Section SI 1) [DePonte et al., 2008]. Filamentous samples entrained in the fluid ejected from this virtual nozzle align via extensional stress to the fluid's convergent streamlines [Brizitsky et al., 1978]. Bright, femtosecond XFEL pulses were used to repeatedly illuminate this filament-laden flow, producing a large number of diffraction patterns each from only tens to hundreds of different filaments. Finally, we extracted a subset of these single-shot patterns that showed sufficiently small disorientation and relatively low solvent scattering, which were averaged to produce a highly aligned fiber diffraction pattern with minimal solvent scattering.

Filaments in this system can be studied in their near-native solvent environment with minimal radiation damage due to the self-shuttering mechanism of ultrafast XFEL pulses [Neutze et al., 2000]. Using actin filaments as a calibration sample, we further computationally re-aligned the already flow-aligned fiber diffraction patterns with a disorientation half-width-half-max standard deviation of about 5 degrees. This computational procedure re-aligns each noisy actin diffraction pattern to produce an average pattern that in turn maximizes the likelihood of generating the patterns we measured [details in Supplementary SI5]. We show that three other biologically relevant fiber systems flow-align in a similar manner.

Results

Four diverse filament systems were prepared to test the feasibility of studying the structures of periodic biological filament systems with an XFEL. Solutions of these samples were formed into continuous micro-jets focused to various diameters, which were intercepted by the XFEL (Fig. 1). The jet diameter was controlled by the nozzle size, pressure of the liquid in the nozzle, and the rate of gas flow around the nozzle. In

order to minimize the scatter from the jet solvent to vacuum interface, we selected the jet diameter to be larger (4-5 μm) than that of the X-ray beam diameter (0.2 μm or 1 μm). Single-shot diffraction images of these solvated samples were recorded on a CSPAD detector (Figs. 2-5; Supplementary Section SI 2), and then computationally processed and classified. For each sample, only patterns that showed prominent fiber diffraction features were averaged (Supplementary Section SI 3).

Actin

Actin filaments were generated by nucleation [Oosawa and Asakura, 1975] and pointed-end growth from calcium-activated gelsolin [Nag et al., 2013] (Fig. 1A). This procedure produces gelsolin-capped actin filaments in which there is a narrow length distribution. The average length of the filaments can be controlled by the gelsolin to actin ratio. At actin concentrations of 60 μM, using a 5 μm diameter micro-jet and an X-ray illuminated volume of ~0.2 x 0.2 x 5 μm, an estimated average of 100 filaments will fall into the X-ray beam as it intersects the center of the 5 μm diameter micro-jet, if flow-induced crowding effects are neglected. Under these conditions, the protein-to-solvent ratio based on volume is estimated to be ~1:200.

A total of 81,352 diffraction patterns were recorded and 11,244 of these were classified as containing small clusters of aligned filaments with weak background scattering (Fig. 2A). These patterns were averaged giving the pattern shown in Fig. 2B. The averaged pattern showed characteristic reflections of F-actin, namely the 5.9 nm and 5.1 nm layer lines arising from the right and left handed generic helices [Holmes et al., 1990] (Fig. 2C), demonstrating that the filaments remained intact in the micro-jet within the vacuum chamber. These layer lines were faint in single femtosecond snapshots but became more pronounced after unsupervised selection and averaging [Loh and Elser, 2009] (Fig. 2B; Supplementary Section SI 3).

The actin filaments flow-aligned remarkably well, in part due to stable injector conditions (Supplementary Sections SI 4-5), and the resulting X-ray diffraction patterns were used to study the intrinsic fiber disorientation. The average fibril orientation was estimated for each diffraction pattern and the patterns computationally aligned before averaging. Subsequent averaging of the aligned patterns reduced the

disorientation standard deviation to 5 degrees, which represents the intrinsic disorientation as seen in a single shot.

***E. coli* pili**

The second filament system studied was type 1 pili that were sheared from the surface of *E. coli*. Pili are extracellular fibers produced mostly by Gram negative bacteria that are crucial for attachment and survival in the environment, notably during infection in human and other animal hosts. Type 1 pili (and the structurally similar P pili) are largely composed of a stiff helical shaft formed by the polymerization of FimA subunits, with approximately 3 subunits per turn. The pilus shaft is 69 Å wide and can extend to lengths of over 1-2 μm (Fig. 1B) [Brinton, 1965; Hahn et al., 2002]. We injected *E. coli* pili into the XFEL pulses at a concentration of 2.6 mg/ml using a 5 μm diameter micro-jet. Assuming an average pilus is 250 nm long, we estimate approximately 100-150 pili in the X-ray illuminated volume (~ 0.2 x 0.2 x 5 μm) of the micro-jet.

Diffraction patterns obtained (Fig. 3A) and the averaged patterns (Fig. 3B) showed prominent features at the ~ 2.4 nm layer line, ~1.16 nm layer line, and a peak on the equator at 4.2 nm. These features represent the helical repeat, the second order of the helical repeat, and the helical radius (2.5 nm to the center of a FimA subunit, whose width is 2.0-2.5 nm; see Supplementary Sections SI 6-7). The presence and alignment of the pili fibers were qualitatively confirmed by comparison of the averaged XFEL fiber pattern with that of synchrotron-based fiber diffraction image from oriented P pilus fibers (Fig. 3C) [Gong and Makowski, 1992; Bullitt and Makowski, 1995]. Comparison of Figs. 3B and 3C shows a reasonable agreement between features from the two techniques.

AgelN amyloid fibrils

The third filament system studied was a self-assembling peptide derived from a mutant gelsolin, which causes the disease Familial Amyloidosis Finnish-type (FAF) [Solomon et al., 2012]. In this case, a minimal peptide AgelN was synthesized [Fadika and Baumann, 2002]. A solution of AgelN (1 mg/ml) in water produced regular fibrils after shaking for 120 h (Fig. 1C). The improved uniformity in morphology of these fibrils allowed for investigation of their structural assembly. The

fibrils were introduced into the XFEL within a 5 μm micro-jet at a concentration of AgelN of 6 mg/ml and 66270 diffraction patterns recorded (Fig. 4A).

Averaging the best diffraction images indicated reasonably low disorientation and shows a prominent meridional layer line, which is split into a doublet at approximately around 0.497 nm and 0.505 nm, and an equatorial reflection at approximately 1.1 nm (Fig. 4B). These spacings indicate that the FAF fibrils are comprised of β-sheets running along the filament axis, and are stacked with a spacing of 1.1 nm across the filament axis, similar to that observed in other amyloid structures [Wille et al., 2009; Geddes et al., 1968].

G11A α-synuclein

The final filament system studied was α-synuclein fibrils (Fig. 1D) that are known to be present as the main component of Lewy bodies, commonly associated with Parkinson's disease. Several lines of evidence point to an 11-residue segment that spans residues 68-78 of α-synuclein, G11A, as being important for the aggregation and toxicity of the full-length protein [Du et al., 2003; Giasson et al., 2001; El-Agnaf and Irvine, 2000]. Electron micrographs of aggregated G11A show needles with notably straight edges, suggesting they are crystalline to some degree (Fig. 1D). The maximum width of the crystals is 200 nm, which is too small to detect by visible light microscopy. Only larger, fibrillar bundles can be observed under visible light (Supplementary Section SI 8), and attempts to obtain X-ray diffraction patterns using a 1.5 μm diameter focus X-ray beam at the SPring8 beamline 32XU revealed only a single 4.6 Å reflection, spread over a wide arc (Fig. 5D).

The combination of the micro-jet injector and XFEL source gave higher-resolution diffraction from the G11A sample, with patterns ranging from fiber diffraction (Fig. 5A) to a single crystal lattice (Fig. 5B). Most of the diffraction images had properties somewhere between these two extremes, where two or more lattices could be seen having similar orientations. The maximum projection image (Fig. 5C) shows the maximum photon count received per pixel across all the collected diffraction patterns, which is observed as sharp reflections spread to form arcs. This projection enhances the location of the bright intensity peaks that stand out over the diffuse scattering. This indicates crystalline aggregates, with modest orientation from shot to shot. This

suggests that with enough images and appropriate sorting algorithms it might be possible to obtain three-dimensional crystal diffraction data sets.

Discussion

We have demonstrated flow alignment of four different biological filament systems in a liquid micro-jet, and the production of diffraction patterns with femtosecond XFEL pulses. This allowed capture of single-shot diffraction features of ~100 filaments that permitted computational selection of the best single-shot diffraction patterns, which upon averaging gives improved fiber diffraction data.

The results show that the already flow-aligned filaments can be further computationally aligned to a disorientation standard deviation of ~ 5 degrees, that AgelN FAF filaments are comprised of stacked β-sheets, and that the G11A particles range in order from crystalline to fibrillar. The collection of data serially, rather than in bulk, indicates that it may be possible, with appropriate processing, to extract full 3D single crystal diffraction patterns from the data.

Overall, these data suggest that XFEL experiments on filamentous systems may be optimized in two ways: an aligned multifilament mode and a single filament mode. In the aligned multifilament mode there are opportunities to improve the flow alignment by optimizing, particle length, salt concentrations, pH and flow speeds [Oda et al., 1998]. Charged filaments like F-actin have a tendency to form a nematic liquid crystalline phase above a certain critical concentration, which is the basis of alignment in conventional fiber diffraction studies [Onsager, 1949; Flory, 1956]. For example above 150 μM, F-actin forms a uniform liquid crystalline phase, with a measured disorientation standard deviation of the filaments, depending on buffer conditions, between 7 and 15 degrees [Suzuki et al., 1991; Helfer et al., 2005].

In a single filament mode, individual diffraction patterns can be computationally aligned and considerably sharpen the orientation distribution. Computational alignment may be limited by background scattering from the water jet. The background water scattering may be reduced by using a nebulizer that creates an aerosol suspension of solvent covered particles [Bogan et al., 2010], followed by a stack of gas-focusing elements focused particle beams of about 20 μm diameter have

been are readily achieved by this method [Spence et al., 2012], and applied to XFEL imaging of aerosols [Loh et al., 2012].

There are many filament systems in biology, most of which are uncharacterized at the structural level [Uribe and Jay, 2009; Fisher et al., 2008]. Decorated actin or tubulin filaments are potential targets for XFEL-fiber diffraction. A wealth of novel actin-like proteins (ALPs) [Derman et al., 2009] and tubulin-like proteins (TLPs) [Pilhofer et al., 2011] have been discovered in bacteria, which are involved in cellular processes such as DNA segregation, cell division and cell shape maintenance. Most of these filaments are helical. Sequence homology between bacterial ALPs or TLPs is low and filament structures are highly diverse [Popp and Robinson, 2011; Popp et al., 2012], making them excellent targets for fiber diffraction studies. To date only one ALP (ParM-R1) has yielded fiber diffraction data for structure determination, due to its availability through high expression levels in *E. coli* [Popp et al., 2008]. Similarly, analysis of genomic data has identified hundreds of different pilus systems that have not been characterized, either functionally or structurally [Hung et al., 1996; Wurpel et al., 2013]. Only type 1 and P pili, both important virulence factors for urinary tract infections, have been studied in detail [Brinton, 1965; Hahn et al., 2002; Gong and Makowski, 1992; Geibel and Waksman, 2011; Le Trong et al., 2010]. Variations in assembly mechanisms are known to exist among different classes of pili [Zavialov et al., 2007], and structural characterization of the pilus shaft could provide valuable insight into these systems that may help rationalize their function during infections as well as help in engineering for biotechnological applications. Finally, understanding the mechanisms of amyloid fibrils in various human diseases [Rambaran and Serpell, 2008] requires architectural information which may be provided by further development of XFEL fiber diffraction methods.

The overall, the advantages of single filament and XFEL fiber diffraction methods over classical fiber diffraction methods are a requirement for significantly less protein, without the need for time-consuming, difficult, and sometimes unsuccessful, filament alignment protocols, and the opportunity to obtain 3D diffraction data from single filaments. The results presented demonstrate the potential of XFELs to extend the range of filament systems that can be studied by fiber diffraction. Single-shot diffraction patterns were recorded from approximately 100 aligned filaments, showing

the potential to obtain structural information from particles that are too small and heterogeneous to be used in conventional synchrotron diffraction experiments. Taking advantage of the high-throughput imaging of XFELs, the heterogeneous sample preparation of G11A was shown to contain both nano-sized crystals and fibrils. Computational techniques were developed to classify the corresponding diffraction patterns and reduce the disorientation by removing the blurring due to jet instability, in particular to identify changes in the angle of the jet relative to the beam. The diffraction patterns collected indicate the possibility of recording single filament data provided that the solvent background can be significantly reduced. XFEL fiber diffraction may also be capable of providing time resolved data, trapping the structure of intermediate states or following the fates of dynamically unstable filament systems.

Methods

Filament preparation

Actin was prepared according to Spudich and Watt [Spudich and Watt, 1971] with small modifications [Wang et al., 2010] and gelsolin was prepared as described [Nag et al., 2009]. F-actin samples for XFEL fiber diffraction were prepared by adding gelsolin to monomeric actin at a ratio of 1:4000 in the presence of 1 mM $CaCl_2$. Polymerization was initiated by adding KCl (50 mM final concentration) two hours prior to the experiment. The average filament length from the 1:4000 gelsolin:actin ratio is expected to be around 10 µm. Actin concentrations were used between 10-60 µM. Under this regime filaments are in the isotropic phase and did not show any birefringence under the polarizing microscope.

Type 1 pili were isolated from a modified strain of UTI89, an *E. coli* strain isolated from the urine of a urinary tract infection patient [Chen et al., 2006]. Strain SLC-490 is a derivative of UTI89 in which one of the inverted repeats flanking the *fimS* switch (which controls the transcription of the entire fim operon encoding the structural proteins, largely FimA, that make up the pilus) has been mutated so that the strain constitutively expresses type 1 pili (locked ON). The purification of type 1 pili was adapted from [Dodd and Eisenberg, 1982]. Bacteria from a frozen stock were inoculated into a 50 ml LB culture and grown overnight, then added to 8 L of culture and grown for 18 hours at 37°C, shaking at 120 rpm. The bacteria were pelleted at

9,000 x g for 6 minutes at 4°C and resuspended in 2.2 L of 0.5% NaCl for washing. Cells were sedimented and resuspended in 220 ml of 5 mM Tris-HCl, pH 8.0. 100-150 ml of bacteria solution was added to a Moulinex blender to shear the pili from the bacteria. Two minutes of blending was repeated five times, with two minutes of cooling on ice between each round of blending. Bacteria were spun down and the supernatant containing the pili was collected. The supernatant was further centrifuged for 30 minutes at 20,000 rpm (Beckman Coulter NVT-65) to pellet contaminating membrane vesicles and flagella. Due to the *fimS* mutation, SLC-490 did not show a contaminating band of flagella by SDS-PAGE analysis; thus the supernatant was directly centrifuged at 53,000 rpm in a NVT-65 for 2 h to pellet the pili. The supernatant was removed and the gelatinous pili pellet was stored in 260 μg (as determined by the Bradford assay) aliquots at –80°C. Prior to the introduction into the micro-jet the pili were resuspended in 1% sodium dodecyl sulfate solution.

Gelsolin FAF amyloid fibrils were formed from the synthetic peptide homologous to the amino acids 183-210 of human plasma gelsolin (AgelN, sequence FNNGNCFILDLGNNIHQWCGSNSNRYER) (GenScript) similarly as described (Fadika and Baumann, 2002), where N indicates the amyloid mutation. Briefly, AgelN was dissolved in water at 1 mg/ml, vortexed, sonicated and incubated for 120 h at room temperature with shaking. These conditions had been optimized to produce consistent morphologies of the filament system as judged by transmission electron microscopy. A drop of filament-containing solution was applied to a carbon-coated copper electron microscopy grid, blotted, stained with 1% uranyl acetate, and visualized under a JEOL 1010 transmission electron microscope operated at 80 keV, and at a nominal magnification of 60,000 times. Prior to X-ray exposure the sample was concentrated to 6 mg/ml and filtered (stainless steel 10 μm filter).

A mixture of fibrils and crystals were produced from an 11-residue segment of α-synuclein, G11A, spanning residues 68-78 (sequence GAVVTGVTAVA). To prepare the sample, ten batches of synthesized peptide (CSBio), 1 mg each, were weighed and each dissolved in 1 mL of sterile water. The samples were shaken at 37°C on a Torrey Pines orbital mixing plate at speed setting 9, overnight. The insoluble material was washed in 30% (w/v) glycerol then stored at room temperature before the diffraction

experiment. Diffraction experiments were performed using a concentration of approximately 25 µl of pelleted material suspended in 1 ml water. Negatively stained G11A specimens for transmission electron microscopy (TEM) were prepared by applying 5 µL of sample on hydrophilic 400 mesh carbon-coated formvar support films mounted on copper grids (Ted Pella, Inc.). These samples were allowed to adhere for 3 min, rinsed twice with distilled water and stained for 1 min with 1% uranyl acetate. Grids were examined on either a JEM1200-EX (JEOL) or T12 (FEI) microscope.

XFEL data collection

The Multiple Nozzle Injector System developed at CFEL (Center for Free-Electron Laser, Hamburg, Germany), which allows for the remote rapid changeover of six nozzles and positioning within 10 nm, was incorporated into the nanofocus chamber of the Coherent X-ray Imaging (CXI) instrument [Boutet and Williams, 2010] at the Linac Coherent Light Source (LCLS) [Emma et al., 2010]. Using a liquid micro-jet formed with a Gas Dynamic Virtual Nozzle (GDVN) [DePonte et al., 2008] the filament systems in their buffer solutions were injected into the XFEL beam with typical velocities of 10 m/s. Single shot diffraction patterns were recorded using a CSPAD detector at 120 Hz by intersecting the jet with a 200 nm x 200 nm XFEL beam of the CXI instrument at LCLS [Boutet et al., 2012]. Actin, amyloids and pili were equilibrated at room temperature before injection into the vacuum chamber of the XFEL beam (Supplementary Section SI 1). The X-ray wavelength was set to 2.07 Å (6 keV), with each X-ray pulse lasting approximately 33 fs. The sample to detector distance was 565 mm for the actin and pili filament systems, and moved to 175 mm for the gelsolin FAF amyloids and 85 mm for the α-synuclein amyloids. The α-synuclein amyloids were imaged with 8.52 keV (1.45 Å) X-ray pulses, each approximately 40 fs in duration, focused to a beam diameter of approximately 1 µm. The micro-jet width was approximately 4 µm and the flow rate was 40 µl/min.

XFEL data processing

More than 10^4 detector exposures (images) of each randomly injected sample type were collected. The processing, selection, and calibration of single snapshots and averaged diffraction patterns for pili, actin and gelsolin are described in the

Supplemental Information, which includes an adaptation of XFEL workflows in the Cheetah processing software [Barty et al., 2014]. The calibration, single stills and composite images for G11A were produced by cctbx.xfel [Hattne et al., 2014]. Using a simple clustering scheme, images were excluded that showed strong edge scattering from the jet or negligible filament diffraction signal (Supplementary Section SI 3). Where possible, hundreds of images that contained only background scattering were isolated, and their average subtracted from the average of the signal-containing images.

The degree of disorientation was estimated from the fluctuations of intensity motifs from single multi-filament patterns or from Bayesian inference of the mutual orientation between the patterns (details in Supplementary Section SI 4 and 5, respectively).

Acknowledgements

Portions of this research were carried out at the Linac Coherent Light Source (LCLS) at the SLAC National Accelerator Laboratory. LCLS is an Office of Science User Facility operated for the U.S. Department of Energy Office of Science by Stanford University. D.P., U.G., H.Z., M.L. and R.C.R. were supported by the Biomedical Research Council, Agency for Science, Technology and Research (A*STAR), Singapore. N.D.L. thanks the support from the Lee Kuan Yew Postdoctoral Fellowship, as well as insightful discussions with Kartik Ayyer, Hugh Philipp and Mark Tate. S.L.C. and L.T.L. are supported by the National Research Foundation, Prime Minister's Office, Singapore under its NRF Research Fellowship Scheme (NRF Award No. NRF-RF2010-10) and the Genome Institute of Singapore (GIS)/A*STAR. A.S.B., J.H. and N.K.S. are supported by NIH/NIGMS grant R01-GM102520. C.G. thanks the PIER Helmholtz Graduate School and the Helmholtz Association for financial support. D.O. acknowledges support from the BMBF through the Röntgen-Angström-Cluster (grant 05K12GU3). J.P.J.C. was supported by a University of Canterbury Doctoral Scholarship. R.P.M. was supported by a James Cook Research Fellowship and a N.Z. Marsden Fund grant. We thank Sabine Botha, Robert L. Shoeman, and Ilme Schlichting for contributing and operating the injector during the G11A LCLS experiment, as well as Kunio Hirata for assisting with G11A diffraction

at SPring8 BL32XU. Financial support from the Knut and Alice Wallenberg Foundation, the Swedish research council and STINT are gratefully acknowledged.

References

Arnott, S. in *Fiber Diffraction Methods* Vol. 141 *ACS Symposium Series* (eds A.D. French & K.H. Gardner) 1-30 (1980).

Barty, A. *et al.* Cheetah: software for high-throughput reduction and analysis of serial femtosecond X-ray diffraction data. *J. Appl. Crystallogr.* **47**, 1118–1131, (2014).

Bernal, J. D. & Fankuchen, I. X-ray and crystallographic studies of plant virus preparations : I. Introduction and preparation of specimens II. Modes of aggregation of the virus particles. *J. Gen. Physiol.* **25**, 111-146, (1941).

Bogan, M., Starodub, D., Hampton, C. Y. & Sierra R. G. Single Particle Coherent Diffractive Imaging with a Soft X-ray Free Electron Laser: Towards Soot Aerosol Morphology. *J. Phys. B* **43**, 194013, (2010).

Boutet, S. & Williams, G. J. The Coherent X-ray Imaging (CXI) instrument at the Linac Coherent Light Source (LCLS). *New J. Phys.* **12**, (2010).

Boutet, S. *et al.* High-resolution protein structure determination by serial femtosecond crystallography. *Science* **337**, 362-364, (2012).

Bragg, W. L. The diffraction of short electromagnetic waves by a crystal. *Proc. Cambridge Philos. Soc.* **17**, 43-57, (1913).

Brinton, C. C., Jr. The structure, function, synthesis and genetic control of bacterial pili and a molecular model for DNA and RNA transport in gram negative bacteria. *Trans. N. Y. Acad. Sci.* **27**, 1003-1054, (1965).

Brizitsky, V. I., Vinogradov, G. V., Isayev, A. I. & Podolsky, Y. Y. Extensional stresses during polymer flow in ducts. *J. Appl. Polym. Sci.* **22**, 751–767 (1978).

Bullitt, E. & Makowski, L. Structural polymorphism of bacterial adhesion pili. *Nature* **373**, 164-167, (1995).

Chen, S. L. *et al.* Identification of genes subject to positive selection in uropathogenic strains of Escherichia coli: a comparative genomics approach. *Proc. Natl. Acad. Sci. U. S. A.* **103**, 5977-5982, (2006).

DePonte, D. P. *et al.* Gas dynamic virtual nozzle for generation of microscopic droplet streams. *J. Phys. D Appl. Phys.* **41**, 195505, (2008).

Derman, A. I. *et al.* Phylogenetic analysis identifies many uncharacterized actin-like proteins (Alps) in bacteria: regulated polymerization, dynamic instability and treadmilling in Alp7A. *Mol. Microbiol.* **73**, 534-552, (2009).

Dodd, D. C. & Eisenstein, B. I. Antigenic quantitation of type 1 fimbriae on the surface of Escherichia coli cells by an enzyme-linked immunosorbent inhibition assay. *Infect. Immun.* **38**, 764-773, (1982).

Du, H. N. *et al.* A peptide motif consisting of glycine, alanine, and valine is required for the fibrillization and cytotoxicity of human alpha-synuclein. *Biochemistry* **42**, 8870-8878, (2003).

El-Agnaf, O. M. & Irvine, G. B. Review: formation and properties of amyloid-like fibrils derived from alpha-synuclein and related proteins. *J. Struct. Biol.* **130**, 300-309, (2000).

Emma, P. *et al.* First lasing and operation of an angstrom-wavelength free-electron laser. *Nat. Photonics* **4**, 641-647, (2010).

Fadika, G. O. & Baumann, M. Peptides corresponding to gelsolin derived amyloid of the finnish type (AGelFIN) adopt two distinct forms in solution of which only one can polymerize into amyloid fibrils and form complexes with apoE. *Amyloid* **9**, 75-82, (2002).

Fisher, K. H., Deane, C. M. & Wakefield, J. G. The functional domain grouping of microtubule associated proteins. *Commun. Integr. Biol.* **1**, 47-50, (2008).

Flory, P. J. Phase equilibria in solutions of rod-like particles. *Proc. R. Soc. A.* **234**, 73-89, (1956).

Franklin, R. E. & Gosling, R. G. Molecular configuration in sodium thymonucleate. *Nature* **171**, 740-741, (1953).

Friedrich, W., Knipping, P. & Laue, M. Interferenz-Erscheinungen bei Röntgenstrahlen. *Sitz. Ber. Akad. Wiss. Munchen.* **42**, 303-322, (1912).

Geddes, A. J., Parker, K. D., Atkins, E. D. & Beighton, E. "Cross-beta" conformation in proteins. *J. Mol. Biol.* **32**, 343-358, (1968).

Geibel, S. & Waksman, G. Crystallography and electron microscopy of chaperone/usher pilus systems. *Adv. Exp. Med. Biol.* **715**, 159-174, (2011).

Giasson, B. I., Murray, I. V., Trojanowski, J. Q. & Lee, V. M. A hydrophobic stretch of 12 amino acid residues in the middle of alpha-synuclein is essential for filament assembly. *J. Biol. Chem.* **276**, 2380-2386, (2001).

Gong, M. & Makowski, L. Helical structure of P pili from Escherichia coli. Evidence from X-ray fiber diffraction and scanning transmission electron microscopy. *J. Mol. Biol.* **228**, 735-742, (1992).

Hahn, E. *et al.* Exploring the 3D molecular architecture of Escherichia coli type 1 pili. *J. Mol. Biol.* **323**, 845-857, (2002).

Hattne, J. *et al.* Accurate macromolecular structures using minimal measurements from X-ray free-electron lasers. *Nat. Methods* **11**, 545-548, (2014).

Helfer, E., Panine, P., Carlier, M. F. & Davidson, P. The interplay between viscoelastic and thermodynamic properties determines the birefringence of F-actin gels. *Biophys. J.* **89**, 543-553, (2005).

Holmes, K. C. & Blow, D. M. The use of x-ray diffraction in the study of protein and nucleic acid structure. *Methods Biochem. Anal.* **13**, 113-239, (1965).

Holmes, K. C., Popp, D., Gebhard, W. & Kabsch, W. Atomic model of the actin filament. *Nature* **347**, 44-49, (1990).

Hung, D. L., Knight, S. D., Woods, R. M., Pinkner, J. S. & Hultgren, S. J. Molecular basis of two subfamilies of immunoglobulin-like chaperones. *EMBO J.* **15**, 3792-3805, (1996).

Huxley, H. E. X-ray analysis and the problem of muscle. *Proc. R. Soc. Lond. B. Biol. Sci.* **141**, 59-62, (1953).

Klug, A., Crick, F. H. C. & Wyckoff, H. W. Diffraction by helical structures. *Acta Crystallogr.* **11**, 199-213, (1958).

Le Trong, I. *et al.* Donor strand exchange and conformational changes during E. coli fimbrial formation. *J. Struct. Biol.* **172**, 380-388, (2010).

Loh, N. T. & Elser, V. Reconstruction algorithm for single-particle diffraction imaging experiments. *Phys. Rev. E Stat. Nonlin. Soft Matter Phys.* **80**, 026705, (2009).

Loh, N. D. *et al.* Fractal morphology, imaging and mass spectrometry of single aerosol particles in flight. *Nature* **486**, 513-517, (2012).

Millane, R. P. in *International Tables for Crystallography IUCr.* **Ch. 4.5**, 568-583, (2010),

Nag, S. *et al.* Ca2+ binding by domain 2 plays a critical role in the activation and stabilization of gelsolin. *Proc. Natl. Acad. Sci. U. S. A.* **106**, 13713-13718, (2009).

Nag, S., Larsson, M., Robinson, R. C. & Burtnick, L. D. Gelsolin: The tail of a molecular gymnast. *Cytoskeleton (Hoboken)* **70**, 360-384, (2013).

Namba, K. & Stubbs, G. Structure of tobacco mosaic virus at 3.6 Å resolution: implications for assembly. *Science* **231**, 1401-1406, (1986).

Neutze, R., Wouts, R., van der Spoel, D., Weckert, E. & Hajdu, J. Potential for biomolecular imaging with femtosecond X-ray pulses. *Nature* **406**, 752-757, (2000).

Oda, T., Makino, K., Yamashita, I., Namba, K. & Maeda, Y. Effect of the length and effective diameter of F-actin on the filament orientation in liquid crystalline sols measured by x-ray fiber diffraction. *Biophys. J.* **75**, 2672-2681, (1998).

Oda, T., Iwasa, M., Aihara, T., Maeda, Y. & Narita, A. The nature of the globular- to fibrous-actin transition. *Nature* **457**, 441-445, (2009).

Onsager, L. The effects of shape on the interaction of colloidal particles. *Ann. N. Y. Acad. Sci.* **51**, 627-659, (1949).

Oosawa, F., Asakura. S. Thermodynamics of the polymerization of proteins. Academic Press 91975).

Pilhofer, M., Ladinsky, M. S., McDowall, A. W., Petroni, G. & Jensen, G. J. Microtubules in bacteria: Ancient tubulins build a five-protofilament homolog of the eukaryotic cytoskeleton. *PLoS Biol.* **9**, e1001213, (2011).

Polanyi, M. Das Röntgen-Faserdiagramm (Erste Mitteilung) *Z. Phys.* **7**, 149-180, (1921).

Polanyi, M. & Weissenberg, K. Das Röntgen-Faserdiagramm (Zweite Mitteilung) *Z. Phys.* **9**, 123-130, (1923).

Popp, D., Lednev, V. V. & Jahn, W. Methods of preparing well-orientated sols of f-actin containing filaments suitable for X-ray diffraction. *J. Mol. Biol.* **197**, 679-684, (1987).

Popp, D. *et al.* Molecular structure of the ParM polymer and the mechanism leading to its nucleotide-driven dynamic instability. *EMBO J.* **27**, 570-579, (2008).

Popp, D. & Robinson, R. C. Many ways to build an actin filament. *Mol. Microbiol.* **80**, 300-308, (2011).

Popp, D. *et al.* Novel actin-like filament structure from Clostridium tetani. *J. Biol. Chem.* **287**, 21121-21129, (2012).

Rambaran, R. N. & Serpell, L. C. Amyloid fibrils: abnormal protein assembly. *Prion* **2**, 112-117, (2008).

Spence, J. C., Weierstall, U. & Chapman, H. N. X-ray lasers for structural and dynamic biology. *Rep. Prog. Phys.* **75**, 102601, (2012).

Solomon, J. P., Page, L. J., Balch, W. E. & Kelly, J. W. Gelsolin amyloidosis: genetics, biochemistry, pathology and possible strategies for therapeutic intervention. *Crit. Rev. Biochem. Mol. Biol.* **47**, 282-296, (2012).

Spudich, J. A. & Watt, S. The regulation of rabbit skeletal muscle contraction. I. Biochemical studies of the interaction of the tropomyosin-troponin complex with actin and the proteolytic fragments of myosin. *J. Biol. Chem.* **246**, 4866-4871, (1971).

Suzuki, A., Maeda, T. & Ito, T. Formation of liquid crystalline phase of actin filament solutions and its dependence on filament length as studied by optical birefringence. *Biophys. J.* **59**, 25-30, (1991).

Uribe, R. & Jay, D. A review of actin binding proteins: new perspectives. *Mol. Biol. Rep.* **36**, 121-125, (2009).

Wang, H., Robinson, R. C. & Burtnick, L. D. The structure of native G-actin. *Cytoskeleton (Hoboken)* **67**, 456-465, (2010).

Watson, J. D. & Crick, F. H. Molecular structure of nucleic acids; a structure for deoxyribose nucleic acid. *Nature* **171**, 737-738, (1953).

Wilkins, M. H., Stokes, A. R. & Wilson, H. R. Molecular structure of deoxypentose nucleic acids. *Nature* **171**, 738-740, (1953).

Wille, H. *et al.* Natural and synthetic prion structure from X-ray fiber diffraction. *Proc. Natl. Acad. Sci. U. S. A.* **106**, 16990-16995, (2009).

Wurpel, D. J., Beatson, S. A., Totsika, M., Petty, N. K. & Schembri, M. A. Chaperone-usher fimbriae of Escherichia coli. *PLoS One* **8**, e52835, (2013).

Yamashita, I. *et al.* Structure and switching of bacterial flagellar filaments studied by X-ray fiber diffraction. *Nat. Struct. Biol.* **5**, 125-132, (1998a).

Yamashita, I., Suzuki, H. & Namba, K. Multiple-step method for making exceptionally well-oriented liquid-crystalline sols of macromolecular assemblies. *J. Mol. Biol.* **278**, 609-615, (1998b).

Zavialov, A., Zav'yalova, G., Korpela, T. & Zav'yalov, V. FGL chaperone-assembled fimbrial polyadhesins: anti-immune armament of Gram-negative bacterial pathogens. *FEMS Microbiol. Rev.* **31**, 478-514, (2007).

Figure Legends

Figure 1 Flow alignment of filamentous samples in the Gas Dynamic Virtual Nozzle (GDVN). **Top:** Schematic of the GDVN, where a suspension of filamentous samples inside a capillary is focused into a micro-jet in the high-vacuum X-ray imaging chamber using a virtual nozzle formed by a co-axial gas flow. Extended filaments flow-align because of differential flow speeds within the virtual nozzle. **Bottom:** Filament systems used in these studies. **A)** Electron micrograph of F-actin filaments formed by polymerizing G-actin with 50 mM KCl for 2 hours in the presence of gelsolin (4000:1). **B)** Electron micrograph of type I pili that were sheared from the surface of *E. coli.* **C)** Electron micrograph of AgelN amyloid fibrils formed in water after 5 days of incubation. **D)** Electron micrograph showing the needle-like appearance of the G11A aggregates.

Figure 2 XFEL fiber diffraction from actin filaments colored according to photon intensity per detector pixel. **A)** A total of 52738 patterns were collected and 26,610 were classified as usable (small or medium cluster of aligned filaments), the remainder containing large, non-oriented clusters of filaments or strong background scattering. **B)** An averaged XFEL fiber diffraction from the selected images that shows the most prominent layer lines. The 5.96 nm (order l=6) and 5.1 nm (order l=7) layer lines are clearly visible, which arise from the protomer spacing in the right and left handed long and short pitches of the actin helix, respectively. **Boxes 1-3**) Weaker, higher-order layer lines are also labeled and enhanced for contrast (e.g. 2.98 nm (order l=13) layer line, which arises from the separation of the long pitch actin strands). **Box 4**) shows detector artifacts, and **Box 5)** shows spurious scattering from upstream optics. **C)** Qualitative comparison against features from a fiber diffraction pattern collected from capillary aligned F-actin collected on a rotating anode X-ray generator.

Figure 3 XFEL fiber diffraction from *E. coli* type 1 pili colored according to photon intensity per detector pixel. **A)** 81352 such patterns were either classified as usable (containing a small cluster of aligned filaments) or unusable (large non-oriented clusters of filaments; strong scattering from edges of micro-jet; strong background scattering). Only the most intense, usable patterns were selected and averaged. **B)** An

averaged XFEL fiber diffraction from 11,244 images that shows the most prominent layer lines. The 2.44 nm layer lines indicate the pitch of the helical pili. Additional reference rings (4.25, 2.6, 1.77 and 1.16 nm) shown here aid comparison with classical pattern in C. Relevant features are boxed. **Box 1)** the equatorial intensity at 4.2 nm, **Box 2)** the 2.44 nm layer line, and **Box 3)** the 1.16 nm layer line. Boxes 2 and 3 have been enhanced for contrast. **C)** Qualitative features of synchrotron-based fiber diffraction pattern collected from capillary aligned P pili from *E. coli* strain Cla-pRHU845. The same resolution guides as in panel (**B**) are shown.

Figure 4 XFEL fiber diffraction from AgelN amyloid fibrils colored according to photon intensity per detector pixel. **A)** Four XFEL fiber diffraction patterns from single femtosecond pulses of photons of X-ray wavelength 2.0664 Å. 66270 such patterns were classified as either usable (small or medium cluster of aligned filaments) or unusable (medium, large non-oriented clusters of filaments). Only the most intense, usable patterns were selected and averaged. **B)** An averaged XFEL fiber diffraction pattern from 48747 images that shows the most prominent layer lines. **Box 1)** 0.505 and 0.497 nm meridional layer lines arising from the amyloid fibrils' β-strand stacking. The strong equatorial intensity in **Boxes 2)** and **3)** at 1.1 nm arises from β-sheet stacking. **Inset)** An enlargement of the 0.505 and 0.497 nm meridional layer lines.

Figure 5: XFEL fiber diffraction from G11A aggregates. **A)** An example of a single diffraction pattern from the most fibrillar aggregates. **B)** An example of a single diffraction pattern from the most crystalline, single, G11A aggregates. The Miller indices are indicated. **C)** A maximum projection computed using all diffraction patterns of a single run. **D)** The best diffraction pattern that could be obtained using a 1.5 μm focus beam at a third-generation synchrotron and sample mounted in a loop.

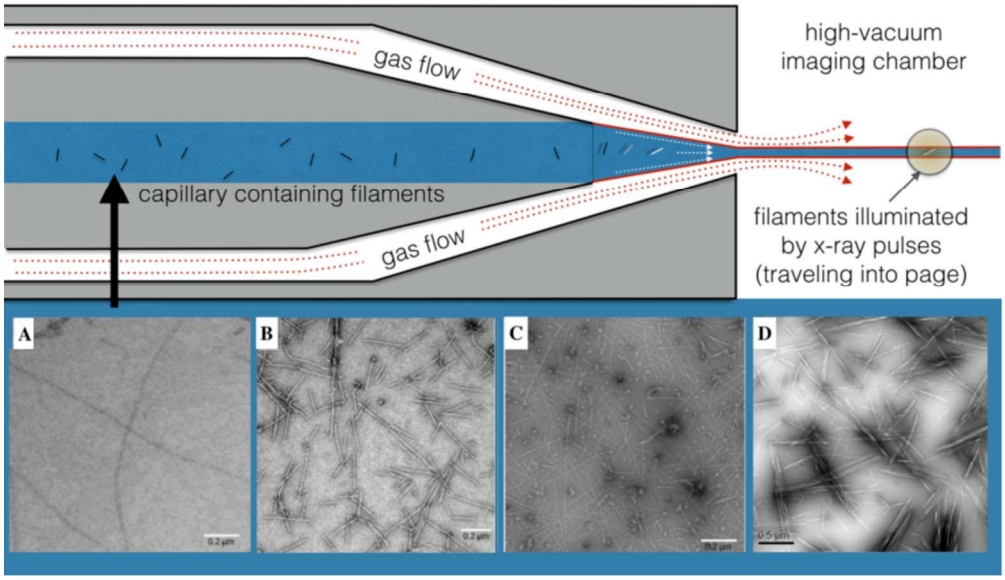

Figure 1 Flow alignment of filamentous samples in the Gas Dynamic Virtual Nozzle (GDVN). Top: Schematic of the GDVN, where a suspension of filamentous samples inside a capillary is focused into a micro-jet in the high-vacuum X-ray imaging chamber using a virtual nozzle formed by a co-axial gas flow. Extended filaments flow-align because of differential flow speeds within the virtual nozzle. Bottom: Filament systems used in these studies. A) Electron micrograph of F-actin filaments formed by polymerizing G-actin with 50 mM KCl for 2 hours in the presence of gelsolin (4000:1). B) Electron micrograph of type I pili that were sheared from the surface of E. coli. C) Electron micrograph of AgelN amyloid fibrils formed in water after 5 days of incubation. D) Electron micrograph showing the needle-like appearance of the G11A aggregates.

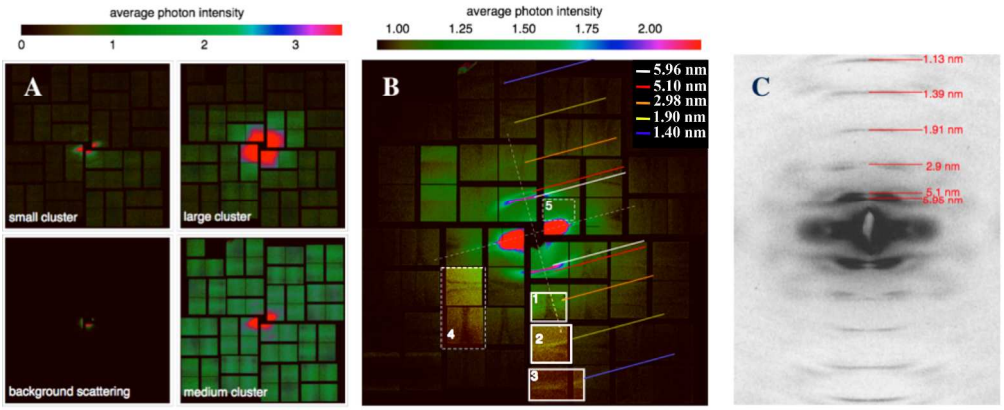

Figure 2 XFEL fiber diffraction from actin filaments colored according to photon intensity per detector pixel. A) A total of 52738 patterns were collected and 26,610 were classified as usable (small or medium cluster of aligned filaments), the remainder containing large, non-oriented clusters of filaments or strong background scattering. B) An averaged XFEL fiber diffraction from the selected images that shows the most prominent layer lines. The 5.96 nm (order l=6) and 5.1 nm (order l=7) layer lines are clearly visible, which arise from the protomer spacing in the right and left handed long and short pitches of the actin helix, respectively. Boxes 1-3) Weaker, higher-order layer lines are also labeled and enhanced for contrast (e.g. 2.98 nm (order l=13) layer line, which arises from the separation of the long pitch actin strands). Box 4) shows detector artifacts, and Box 5) shows spurious scattering from upstream optics. C) Qualitative comparison against features from a fiber diffraction pattern collected from capillary aligned F-actin collected on a rotating anode X-ray generator.

359x151mm (300 x 300 DPI)

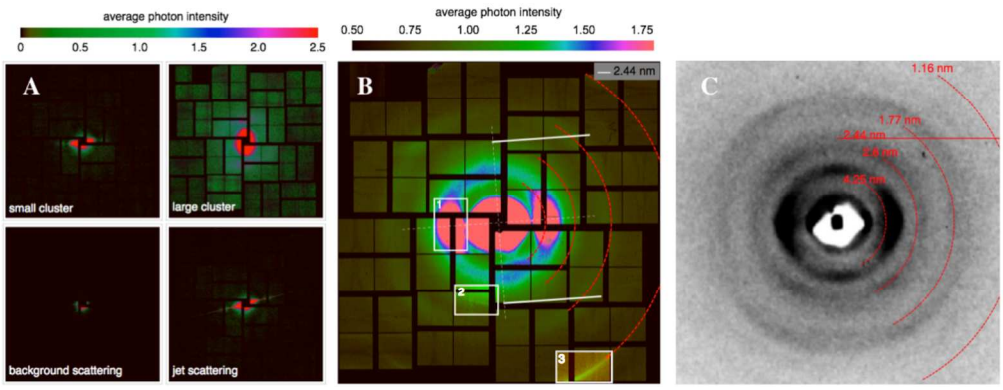

Figure 3 XFEL fiber diffraction from E. coli type 1 pili colored according to photon intensity per detector pixel. A) 81352 such patterns were either classified as usable (containing a small cluster of aligned filaments) or unusable (large non-oriented clusters of filaments; strong scattering from edges of micro-jet; strong background scattering). Only the most intense, usable patterns were selected and averaged. B) An averaged XFEL fiber diffraction from 11,244 images that shows the most prominent layer lines. The 2.44 nm layer lines indicate the pitch of the helical pili. Additional reference rings (4.25, 2.6, 1.77 and 1.16 nm) shown here aid comparison with classical pattern in C. Relevant features are boxed. Box 1) the equatorial intensity at 4.2 nm, Box 2) the 2.44 nm layer line, and Box 3) the 1.16 nm layer line. Boxes 2 and 3 have been enhanced for contrast. C) Qualitative features of synchrotron-based fiber diffraction pattern collected from capillary aligned P pili from E. coli strain Cla-pRHU845. The same resolution guides as in panel (B) are shown.

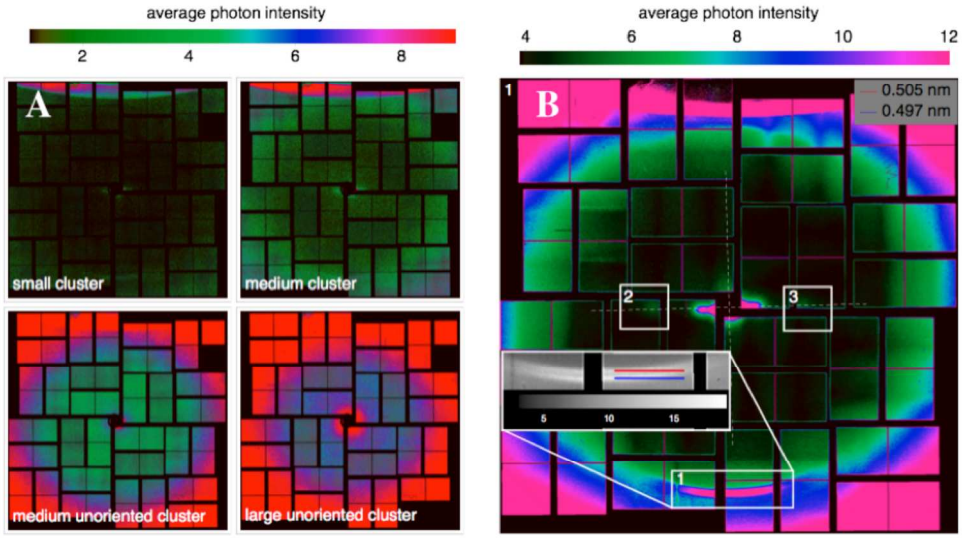

Figure 4 XFEL fiber diffraction from AgeIN amyloid fibrils colored according to photon intensity per detector pixel. A) Four XFEL fiber diffraction patterns from single femtosecond pulses of photons of X-ray wavelength 2.0664 Å. 66270 such patterns were classified as either usable (small or medium cluster of aligned filaments) or unusable (medium, large non-oriented clusters of filaments). Only the most intense, usable patterns were selected and averaged. B) An averaged XFEL fiber diffraction pattern from 48747 images that shows the most prominent layer lines. Box 1) 0.505 and 0.497 nm meridional layer lines arising from the amyloid fibrils' β-strand stacking. The strong equatorial intensity in Boxes 2) and 3) at 1.1 nm arises from β-sheet stacking. Inset) An enlargement of the 0.505 and 0.497 nm meridional layer lines.

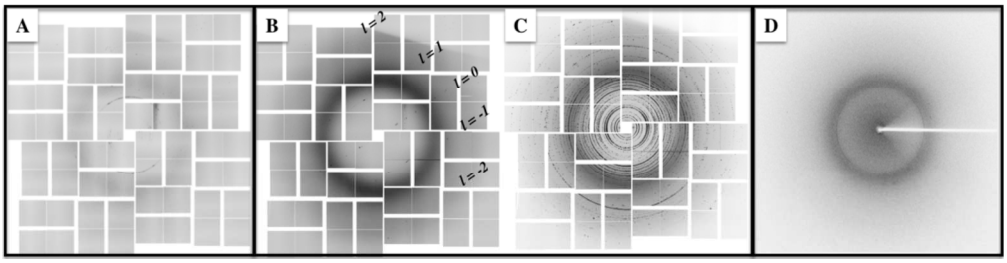

Figure 5: XFEL fiber diffraction from G11A aggregates. A) An example of a single diffraction pattern from the most fibrillar aggregates. B) An example of a single diffraction pattern from the most crystalline, single, G11A aggregates. The Miller indices are indicated. C) A maximum projection computed using all diffraction patterns of a single run. D) The best diffraction pattern that could be obtained using a 1.5 μm focus beam at a third-generation synchrotron and sample mounted in a loop.